A&A 466, 137–149 (2007)
DOI: 10.1051/0004-6361:20066433

Astronomy & Astrophysics

Near-IR imaging of Galactic massive clusters: Westerlund 2⋆,⋆⋆

J. Ascenso[1,2], J. Alves[3], Y. Beletsky[4], and M. T. V. T. Lago[1,2]

[1] Centro de Astrofísica da Universidade do Porto, Rua das Estrelas, 4150-762 Porto, Portugal
e-mail: joanasba@astro.up.pt
[2] Departamento de Matemática Aplicada da Faculdade de Ciências, Universidade do Porto, Rua do Campo Alegre 657, 4169-007 Porto, Portugal
[3] Calar Alto Observatory–Centro Astronómico Hispano-Alemán, C/ Jesús Durbán Remón 2-2, 04004 Almeria, Spain
[4] European Southern Observatory, Karl-Schwarzschild-Str. 2, 85748 Garching, Germany

Received 22 September 2006 / Accepted 21 December 2006

ABSTRACT

Context. Most stars in the Galaxy were formed in massive clusters. To understand nature's favorite mode of star formation and the initial stages of the life of most stars one needs to characterize the youngest and resolved massive clusters in the Milky Way. Unfortunately young massive clusters are challenging observational targets as they are rare, hence found at large distances, are still embedded in their parental molecular cloud, and are swamped by relatively bright nebulae.
Aims. In this paper we propose to use deep subarcsec resolution NIR data to derive the basic parameters of the unstudied population of massive cluster Westerlund 2.
Methods. We present deep JHK_s images (~0.6″ seeing) and photometry of Westerlund 2. This is the most complete photometric census of the cluster's population to date.
Results. We detect a total of 4701, 5724, and 5397 sources in the J, H, and K_s bands respectively. By comparison with main-sequence and pre-main-sequence model tracks, we determine an average visual extinction toward the cluster of 5.8 mag, a likely distance of 2.8 kpc, and an age of 2.0 ± 0.3 Myr for the core of the cluster. Although we have the sensitivity to reach beyond the hydrogen burning limit in the cluster, we are only complete to about 1 $M_\odot$ due to source confusion. We find no evidence for a top-heavy MF, and the slope of the derived mass function is −1.20 ± 0.16. Based on the extrapolation of a field IMF, we roughly estimate the total mass of the cluster to be about 10^4 $M_\odot$. We find compelling evidence for mass segregation in this cluster.

Key words. open clusters and associations: individual: Westerlund 2 – stars: pre-main sequence – infrared: stars

1. Introduction

Young stellar clusters are the basic units of star formation. The clouds' initial conditions and structure, as well as all the process of star formation, are reflected on the clusters' properties given their young age and generally embedded state. Their mass and spatial stellar distributions are the direct consequence of the star formation process and can be used to constrain the models of molecular cloud evolution into stars (Lada & Lada 2003). However, these studies are mostly hampered by the poor knowledge of the basic parameters of each individual cluster, the distance being the most difficult to estimate accurately. In fact, when this parameter is known it is possible to characterize the cluster in terms of its stellar and sub-stellar populations, age spread and star forming history, disk and binary fractions, and, ultimately, determine its mass function which, in young clusters, corresponds approximately to the initial mass function. Over the last decade, the development of sensitive NIR detectors has allowed the study of the youngest, optically invisible clusters with different masses and in different environments (e.g., Lada et al. 1996; Eisenhauer et al. 1998; Muench et al. 2002; Alves & Homeier 2003; Kumar et al. 2003; Liu et al. 2003; Piskunov et al. 2004; Homeier & Alves 2005).

Gum 29 (Gum 1955) (also known as RCW 49, Rodgers et al. 1960), is a large HII region dominated by the compact and massive cluster Westerlund 2 (hereafter W2, Westerlund 1961). The distance measurements in the literature place it between 2 to 8 kpc from the Sun in the direction of the tangent to the Sagittarius-Carina spiral arm of our galaxy. Radio observations and comparison with galactic rotation models yield kinematic distances ranging from 2.3 to 6 kpc (Westerlund 1961; Manchester et al. 1970; Wilson et al. 1970; Gianotti et al. 1972; Goss et al. 1972; Caswell & Haynes 1987; Whiteoak & Uchida 1997). Optical (spectro-)photometric distances that make use of some of the brightest stars in the cluster are also reported ranging from 2.3 to 7.9 (Moffat & Vogt 1975; Moffat et al. 1991; Brand & Blitz 1993; Piatti et al. 1998; Carraro & Munari 2004; Uzpen et al. 2005). Finally, Shara et al. (1991) and Rauw et al. (2005) have determined the distance to the Wolf-Rayet binary star WR20a (see Fig. 2) to be of 4.6−6.3 and 7.9 kpc, respectively. They assume it to be the distance to the cluster although the membership of WR20a is yet to be established. This conflicting distance determinations illustrate well the difficulty in deriving this fundamental parameter accurately.

⋆ Based on observations collected with the SOFI instrument at the NTT at the La Silla Observatory, Chile, under the ESO program 074.C-0728(A).

⋆⋆ The tables with the photometry (Table 2) are only available in electronic form at the CDS via anonymous ftp to cdsarc.u-strasbg.fr (130.79.128.5) or via
http://cdsweb.u-strasbg.fr/cgi-bin/qcat?J/A+A/466/137

Regarding the age of W2, Piatti et al. (1998) first estimated it to be between 2 and 3 Myr using CCD integrated spectroscopy. Later, Carraro & Munari (2004) report an age below 2 Myr using main-sequence evolutionary tracks to fit their UBV photometry, and Rauw et al. (2005) derive an age between 1 and 2 Myr for WR20a.

In this paper we make use of deep NIR images of W2 to expose and analyse for the first time its extended stellar population, and derive the basic parameters for this cluster, such as distance, reddening, star formation history, frequency of NIR excess sources, and mass function. The paper is organized as follows. In Sect. 2 we describe the observations, data reduction and photometry. In Sect. 3 we characterize our data, namely in terms of the luminosity distribution, source density, reddening and excess fraction. Section 4 contains the discussion and determination of the age and distance for the cluster and the description of the mass distribution. Finally, in Sect. 5 we summarize our conclusions.

2. Data

2.1. Observations

The W2 data were taken with SOFI, NTT (La Silla, Chile) in the night of March 18, 2005. The cluster ($10^h24^m01^s$, $-57°45'32''$) was imaged in J, H and K_s with long exposures (12×10, 15×8 and 20×6 s, respectively) for the photometry of the faint stars and short exposures (1.2 s each band) for the bright stars. The long exposures were taken in Large Field Mode (field of view of $4\farcm9 \times 4\farcm9$, pixel scale $\sim 0\farcs288$/pixel) to image the largest possible area of the cluster whereas the short exposures were taken in Small Field Mode (field of view of $2\farcm4 \times 2\farcm4$, resolution $\sim 0\farcs144$/pixel) to image the inner and most concentrated part of the cluster. Due to the optics configuration, this mode is less sensitive thus minimizing the saturation of the brightest stars, mostly concentrated in the central part of the cluster.

We also observed a nearby control field ($10^h18^m01^s$, $-57°15'31''$) which lies at approximately the same Galactic latitude. This field was imaged in Large Field mode in J, H and K_s with the same exposure times as for the science frames.

2.2. Data reduction

The reduction was done with IRAF following the standard procedure: crosstalk correction, flatfield and illumination correction, sky subtraction, registering and averaging of the sub-frames. The offsets between the sub-frames were determined with JITTER. The final J, H and K_s frames were then registered to one another and trimmed at the common area. After the trimming the final area of the images for photometry was $3\farcm67 \times 4\farcm11$ for the long exposures and $1\farcm99 \times 1\farcm61$ for the short exposures. Figure 1 shows the color image of the cluster composed from the three final long exposure frames in K_s (red), H (green) and J (blue).

2.3. Source extraction and photometry

We used IRAF DAOFIND to detect the sources in the images. In the long exposure images the routine searched for sources with a PSF with full width at half maximum (*FWHM*) from 2.3 to 2.4 pixels ($0\farcs66$ to $0\farcs69$) and brighter than 5 times the mean noise of the "empty" regions of each image. For the short exposure images the *FWHM* ranged from 3.5 to 4.5 pixels ($0\farcs50$ to $0\farcs65$) and the detection threshold was taken as 5 times the mean noise in each image. We performed PSF photometry on the stars of the cluster due to crowding in most of the image. This was done with IRAF DAOPHOT. The PSF was chosen from the standard functions defined within IRAF to be the best fit to a set of 22 to 23 stars chosen to be bright and isolated. The best fit was always found for the "Penny" function, a Gaussian core with Lorentzian wings, both for the long and short exposures. The instrumental magnitudes were converted into the Persson et al. (1998) photometric system and from there to the 2MASS[1] photometric system according to the following set of equations: SOFI to Persson (SOFI's user manual):

$$K_P = 1.005(K_s - 0.005J) \quad (1)$$

$$J_P = J - 0.007(J - K_P) \quad (2)$$

$$H_P = H - 0.022(J - K_P) \quad (3)$$

$$(K_s)_P = K_s + 0.023(J - K_P). \quad (4)$$

Persson to 2MASS (Carpenter 2001):

$$(K_s)_2 = (K_s)_P - 0.002(J_P - (K_s)_P) - 0.01 \quad (5)$$

$$H_2 = 1.019H_P - 0.017(K_s)_P - 0.002J_P - 0.005 \quad (6)$$

$$J_2 = 1.005J_P - 0.005(K_s)_P - 0.008 \quad (7)$$

where the subscripts "P" and "2" indicate Persson and 2MASS respectively. The SOFI magnitudes have no subscript.

The magnitudes of 7 to 10 isolated stars spread across the frames were then compared with the 2MASS photometry for the same stars thus obtaining an "instrumental zeropoint" for the magnitude scale that already includes the airmass correction, the mean aperture correction and the actual photometric zeropoint, given that these are all additive quantities to the magnitude scale. These zeropoints were then used to cross-calibrate the magnitude scale of the short exposure images. The "instrumental zeropoints" calculated in this way are summarized in Table 1. The difference in resolution between the 2MASS sample and our own does not influence significantly the calibration as the chosen stars are isolated and do not have bright companions. Perhaps for this reason the mean rms for the calibration are relatively small.

The photometry from the long and short exposures were put together including all the stars from the long exposures (higher signal-to-noise) and those stars from the short exposures that were saturated in the first.

2.4. Completeness limits

The completeness limits were determined for the long exposures by adding artificial stars of increasing magnitudes to the original frames. For each (0.5 mag) magnitude bin the stars were added in fixed positions separated from the adjacent ones by two PSF radii + 1 pixels (PSF radius ~10 pixels) according to the model PSF used for the photometry, thus comprising a grid with the maximum possible number of stars that does not add to the crowding effect. The results are shown in Fig. 3: the sample is 90% complete for $J = 17.88$ mag, $H = 17.00$ mag and $K = 15.52$ mag. The reason for these high completeness limits is the high surface density of sources, leading to blending and some confusion (see next section), and the presence of a non-uniform background (the nebula).

These completeness limits are an average over the whole frame and are not representative of the region close to the center of the cluster where the very high stellar density make the

[1] The Two Micron All Sky Survey is a joint project of the University of Massachusetts and the Infrared Processing and Analysis Center/California Institute of Technology, funded by the National Aeronautics and Space Administration and the National Science Foundation.

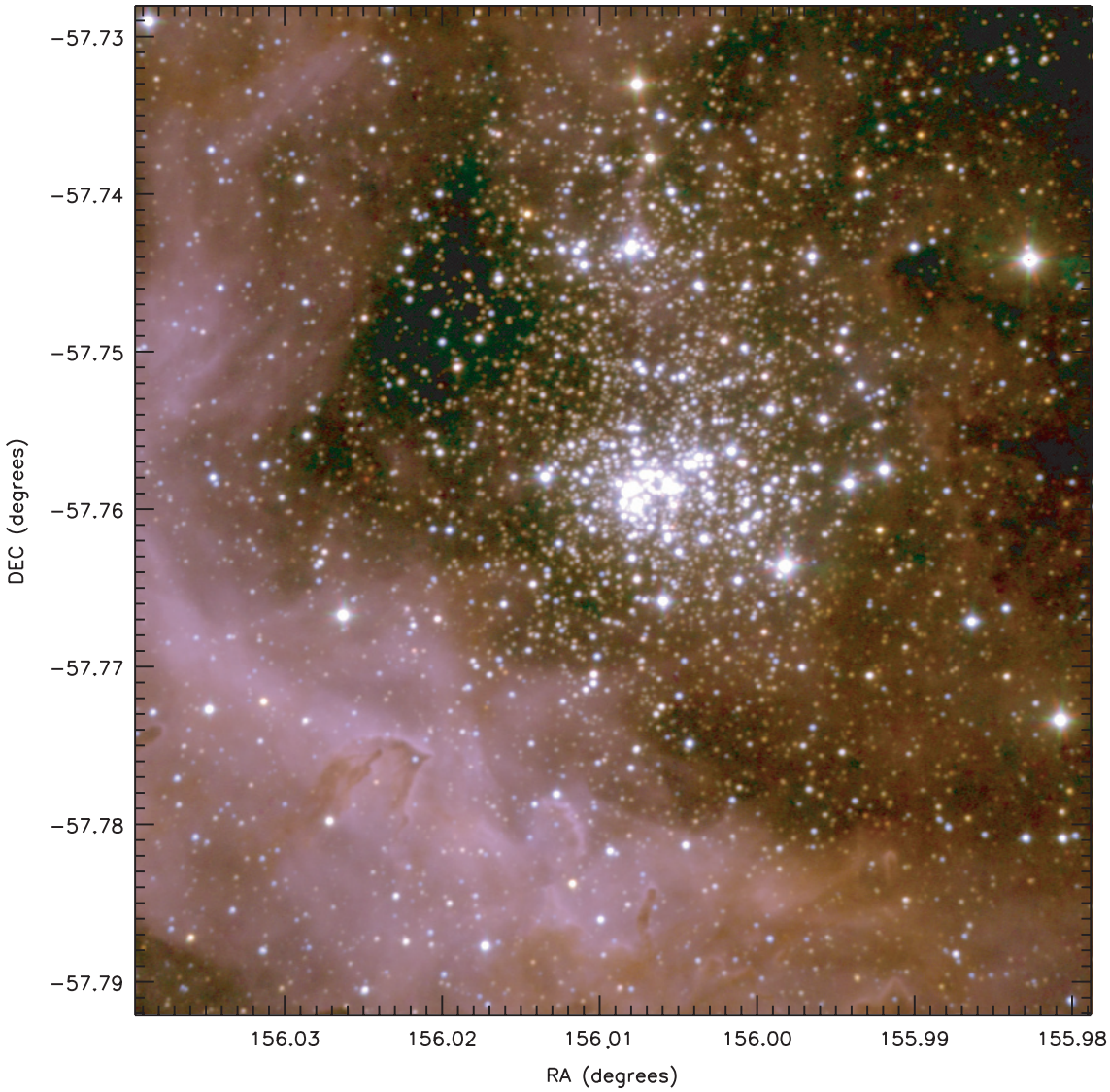

Fig. 1. Color composite of the long-exposure observed field of view in J (blue), H (green) and K_s (red). North is up and East is left.

Table 1. Instrumental zeropoints for the long and short exposure science frames.

	Band	ZP_{inst} (mag)	rms (mag)
Long exp.	J	23.039	0.095
	H	22.941	0.055
	K_s	22.447	0.078
Short exp.	J	22.930	0.087
	H	22.848	0.054
	K_s	22.302	0.025

source detection utterly inefficient. This can only be overcome only with observations with adaptive optics. Our 5-σ sensitivity limits are typically four magnitudes fainter than our completeness limits.

2.5. Accuracy

We used the parameters *sharpness* and *chi* given by ALLSTAR to exclude the stars with "bad" photometry. These parameters measure the roundness of the object and the goodness of the PSF fit and were considered acceptable between −1 and 1 and below 4, respectively. We consider these parameters to be better tracers of photometry quality than the actual "photometric error" from ALLSTAR because they measure directly the geometrical definition of the PSF and how well it represents the actual PSF in the frames, therefore accounting in some way for the residuals left from the subtraction. The "photometric error", on the other hand, depends on many parameters, among which the detector-related properties that are often ill-determined for the combined images. Figures 4 and 5 show the cuts we applied and how they reflect on the "photometric error" for the SOFI data. By performing the cuts in *sharpness* and *chi* we eliminate most of the scatter in the magnitude-error plot while keeping the majority of the objects with an error less than 0.15 mag. If we were to eliminate the stars following a simple "error less than 0.15 mag" criterion we would keep a significant fraction of the objects whose roundness is not typical of stars (e.g., galaxies, blended doubles, hot pixels) or with bad PSF fits and eliminate some with good fits and adequate roundness. The mean photometric errors after the cuts are of 0.06 mag for J and 0.05 mag for H and K_s.

We can also estimate the mean photometric error from the completeness tests by calculating the difference between the input magnitude of the artificial stars and the one measured. This approach is more direct and therefore better, in principle, than

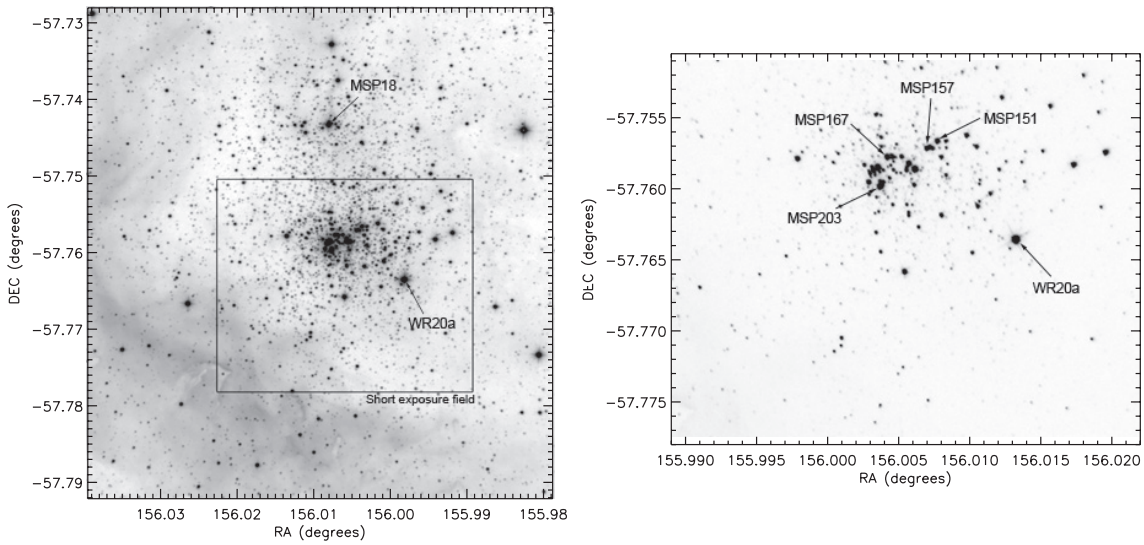

Fig. 2. Comparison of the K_s long- and short-exposures fields of view. The labels indicate the location of the stars WR20a and the ones identified by Moffat et al. (1991).

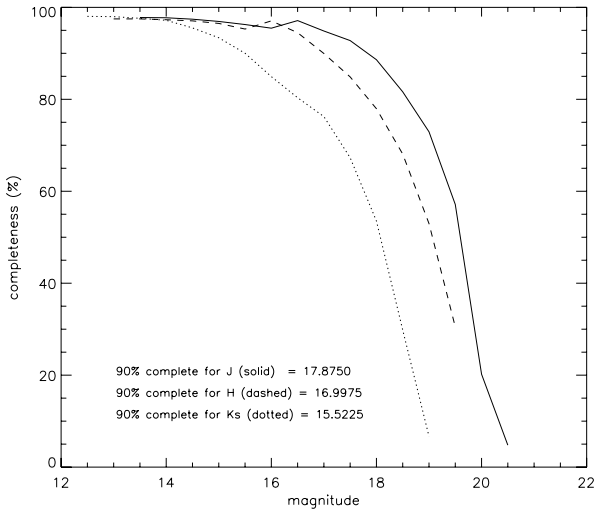

Fig. 3. Variation of completeness with magnitude in the long exposures. We achieve 90% completeness in these images for K_s = 15.5 mag, H = 17.0 mag and J = 17.9 mag.

the one used before. However, this difference is only a measure of the photometric error as long as other sources of error do not dominate. At brightness levels J = 19.5, H = 18.7 and K_s = 18.0 mag for this sample (hereafter blending limits) blending effects begin to be important: the faint artificial stars that are located very close to the brighter underlying stars of the cluster are blended with them and treated as one single object by DAOPHOT with a measured magnitude 10% brighter than the input magnitude. The mean errors from the completeness tests for the stars brighter than the blending limit are 0.04, 0.05 and 0.06 mag in (SOFI) J, H and K_s respectively and are in relatively good agreement with the previously determined values.

The photometric errors in the short exposures are dominated by the distortions in the image so the cuts in *chi* and *sharpness* would not be meaningful. However, since the final sample includes only the brightest stars, for which the errors are small (0.02, 0.04 and 0.03 mag for J, H and K_s respectively), no error cuts are necessary in this sample. Since the distortions are taken into account automatically when constructing the PSF profile the residuals from the PSF subtraction are small.

2.6. Astrometry

The astrometry for the SOFI images was calculated by comparing the positions of some isolated stars with stars in 2MASS. The routines CCMAP and CCSETWCS in IRAF calculated the transformation parameters and applied the transformations to within 0.03″ (1-σ).

3. Results

In the present survey we detect 4701 sources in J, 5724 in H and 5397 in K_s. Although most of the cluster sources are brighter in K_s the number of sources detected in H is larger due to the also larger exposure time.

Even though the distance to the cluster is only discussed in Sect. 4.1 we will use the value of 2.8 kpc whenever necessary.

3.1. Cluster radius and stellar density distribution

Figure 6 shows the radial distribution of the surface density of sources from 2MASS. Only the sources with quality flags A or B in all bands were plotted. We chose to use 2MASS rather than our own sample because our data does not extend beyond a radius of ∼2′ which would be insufficient for a significant analysis of the extent of the cluster. The profile is centered in the peak of the stellar density distribution. As expected, the density is maximum close to the centre and decays into the foreground/background level as the distance to the centre increases. The minimum around 3′ is probably due to the presence of the nebula that sets the detection threshold to higher flux values. This minimum does not allow for an accurate estimate of the cluster's size but the density appears to be flat for radii larger than 5′, 4.1 pc at a distance of 2.8 kpc. However, given the relatively high completeness limits of 2MASS (K_s = 14 mag, see Sect. 3.4), even this value may be underestimated if the fainter, lower-mass population is more widely spread.

Figure 7 shows the 2-D contours for the K_s-band stellar surface density in the surveyed area. The star counts were obtained

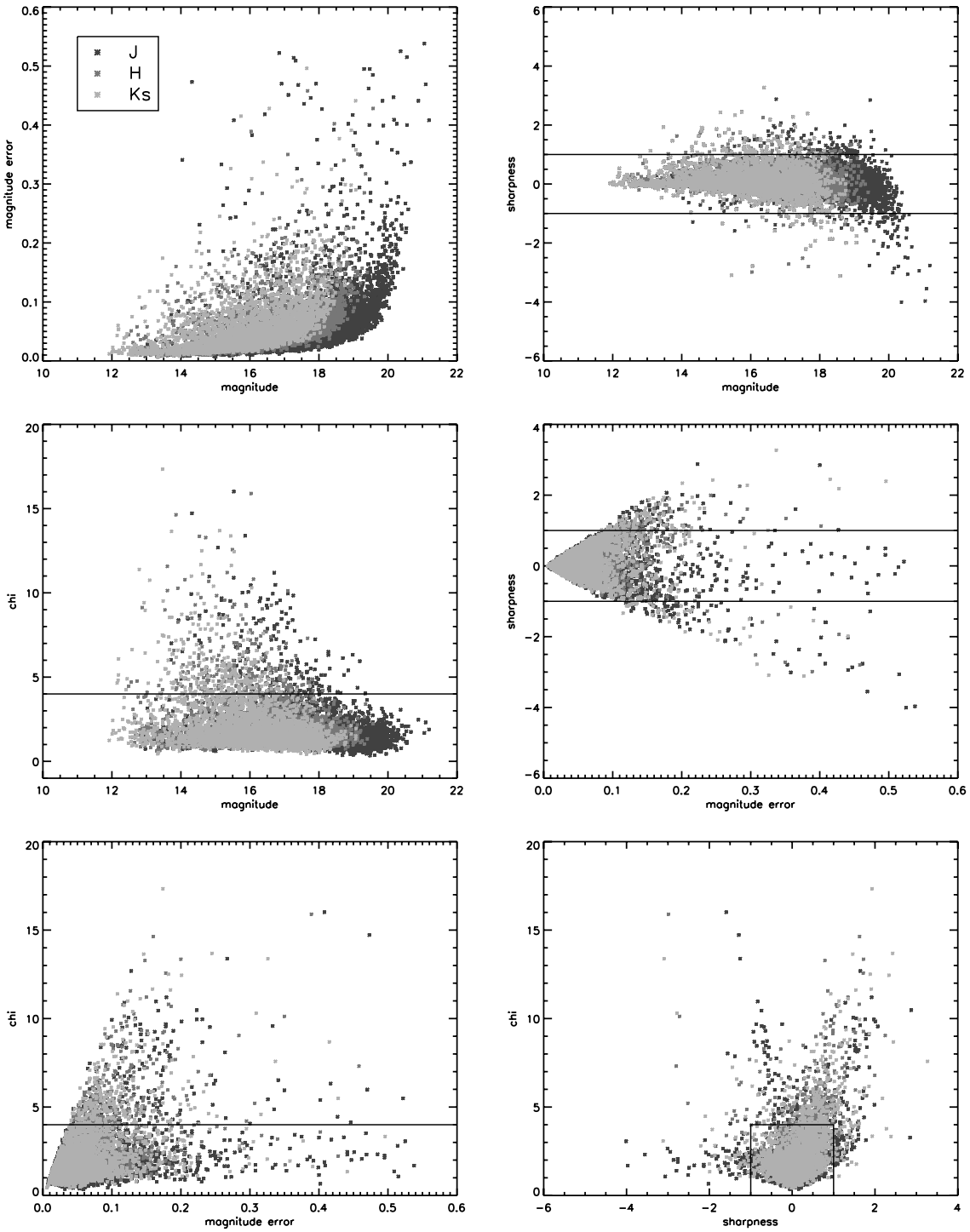

Fig. 4. Error panel for the long exposures. The lines indicate the cuts in *sharpness* and *chi* applied to the raw photometry.

by subdividing the region into a rectilinear grid of overlapping squares, counting the number of stars in each square and dividing by the area of the square. The squares were $12'' \times 12''$ in size and were separated by $6''$, the Nyquist spatial sampling interval. The lowest and highest contours correspond to densities of 25 and 3362 sources/arcmin^2 respectively.

3.2. Reddening

Panel *a* of Fig. 8 shows the $(J - K_s) - K_s$ color−magnitude diagram (CMD) for our field of view. We immediately see that the fainter ($K_s > 14$ mag) sources in our sample are divided into two plumes, presumably the foreground stars in the blue plume and the cluster stars in the redder plume, whereas the brightest ($K_s < 12$ mag) stars are mostly vertically aligned around $(J - K_s) = 0.8$ mag. We have determined the global reddening toward the cluster by fitting the 1 Myr main-sequence isochrone of the Geneva tracks (Lejeune & Schaerer 2001) reddened by some amount to this vertical distribution[2]. Given the lack of

[2] The difference between curves of different ages merely translates into a vertical shift that does not affect the position of the vertical, brightest part of the isochrone and thus the extinction determination.

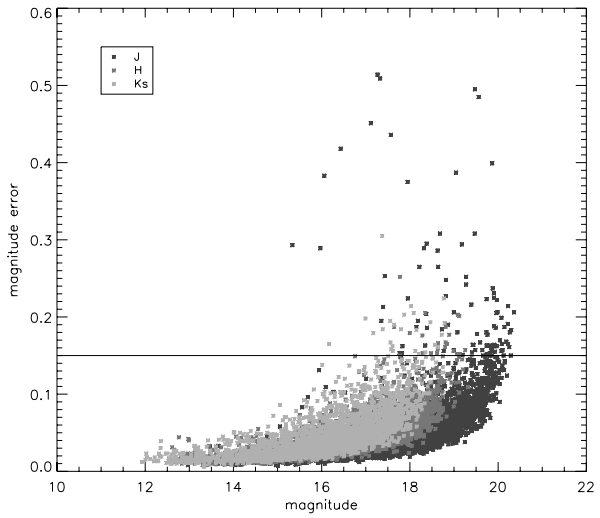

Fig. 5. Photometric errors for the long exposures after the cuts in *sharpness* and *chi*. Most of the sources with error greater than 0.15 mag were discarded (compare with top-left panel in Fig. 4).

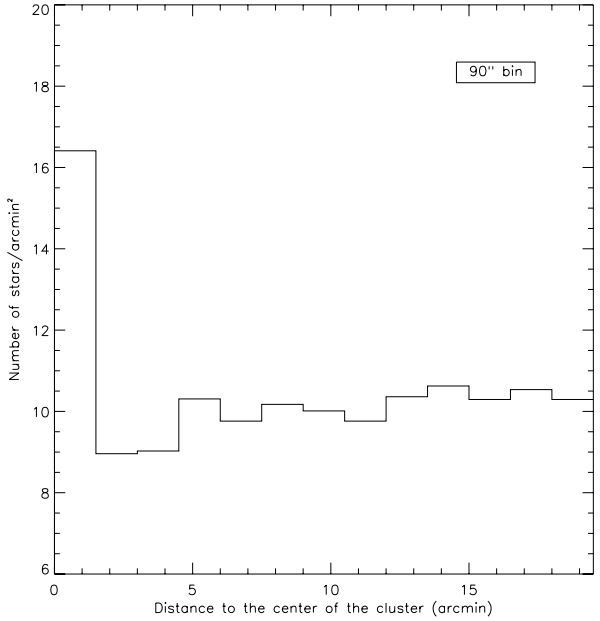

Fig. 6. Radial stellar density distribution from 2MASS $K_s < 14$ mag sources.

information on the metallicity of the cluster we chose to use the models corresponding to the solar value $Z = 0.02$. According to Carraro & Munari (2004) the effect of increasing metallicity is to shift the isochrones toward older ages, larger distances and smaller reddening, although they do not quantify this effect. The effect of extinction is to move objects to fainter magnitudes and redder colors (larger $(J-K_s)$) along the extinction vector defined by the equations (Rieke & Lebofsky 1985):

$$A_v = 5.88((J-K_s)_{\rm int} - (J-K_s)_{\rm obs}) \quad (8)$$

$$(K_s)_{\rm obs} = (K_s)_{\rm int} + 0.112A_v \quad (9)$$

where A_v is the visual extinction and $(J-K_s)_{\rm int}$ and $(J-K_s)_{\rm obs}$ are the intrinsic and observed colors respectively. The light line in panel *a* of Fig. 8 represents the unreddened main-sequence, whereas the dark line represents the same track reddened by $A_v = 5.8 \pm 0.5$ mag, our best fit to the data.

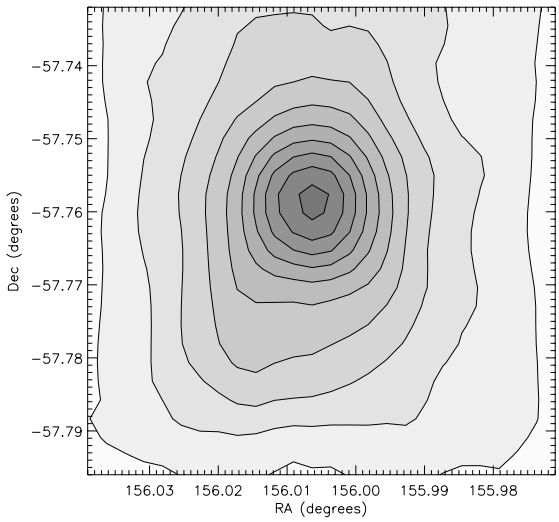

Fig. 7. K_s-band contour plot for the cluster. The lowest and highest contours correspond to densities of 25 and 3362 sources/arcmin^2 respectively.

Having been derived for the brighter stars with little or no scatter in color, this value of extinction represents the overall reddening toward the cluster despite the obvious amount of differential intra-cluster extinction of the fainter, lower-mass stars. This is consistent with the most massive, centrally concentrated members of the cluster having blown a cavity in the cloud thus dissipating most of the gas and dust from the centre, and this having approximately the same line-of-sight extinction. This scenario is confirmed by the images from Spitzer that clearly show a central cavity (Churchwell et al. 2004). The differential extinction within the cluster is generally lower than ∼10 mag.

3.3. Excess sources

The $(H-K_s)/(J-H)$ color–color (CC) diagram for our field of view (Fig. 9, panel *a*) clearly shows two distinct groups of sources, the foreground stars with less extinction and closer to the empiric main sequence dwarf locus, and the cluster population with higher extinction and a greater number of sources. The diagram is color-coded so that the brighter stars appear with a larger symbol and in blue whereas the smaller, red to yellow points represent the fainter sources. The scattering from these two groups increases with increasing magnitude of the sources reflecting the also increasing photometric errors.

In panel *b* of Fig. 9 we show the colors of the cluster (and background) sources. We removed the foreground by conservatively discarding the sources in the bluer plume of the $K_s-(J-K_s)$ color–magnitude diagram in Fig. 8. The overplotted main-sequence on this panel is reddened by $A_v = 5.8$ mag, the global extinction determined in the previous section, and is in good agreement, as expected, with this view of the data. Despite the random scatter we can see an excess of sources to the right of the reddening band indicative of the presence of sources with intrinsic excess emission probably due to circumstellar disks and/or envelopes as would be expected from a young cluster. We derive an estimate of their number by counting the cluster sources that fall to the right of the reddening band and subtracting the number of those that fall to the left to account for the photometric errors in this plot since this area of the CC diagram does not have a physical meaning. We thus count 265 objects with JHK_s excess out of the 2337 objects that likely belong to

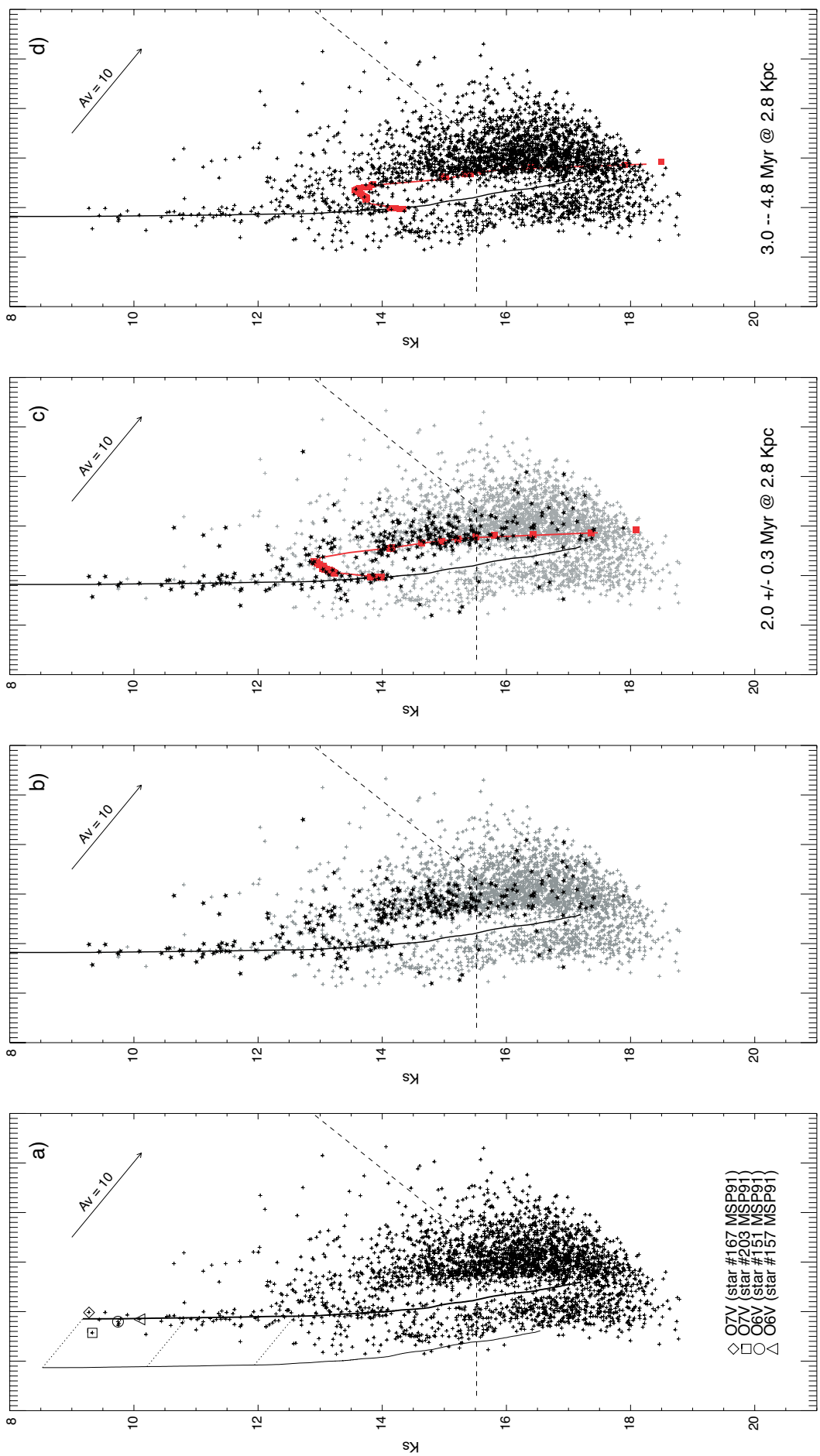

Fig. 8. K_s – $(J - K_s)$ color−magnitude diagram for the cluster. The dashed lines represent the 90% completeness limits of the sample and the vectors represent a visual extinction of 10 mag. **a)** Fit of the reddened (A_v = 5.8 mag) Lejeune & Schaerer (2001) 1-Myr main-sequence isochrone to the brightest stars in the sample. The individual objects are the stars identified by Moffat et al. (1991). **b)** The highlighted (*black stars*) points are located in the inner $1' \times 1'$ square of the science field. **c)** Fit of the Palla & Stahler (1993) PMS models for a range of ages between 1.7 and 2.3 Myr for a distance of 2.8 kpc to the data. **d)** Same as panel **c)** but for a range of ages between 3.0 and 4.8 Myr.

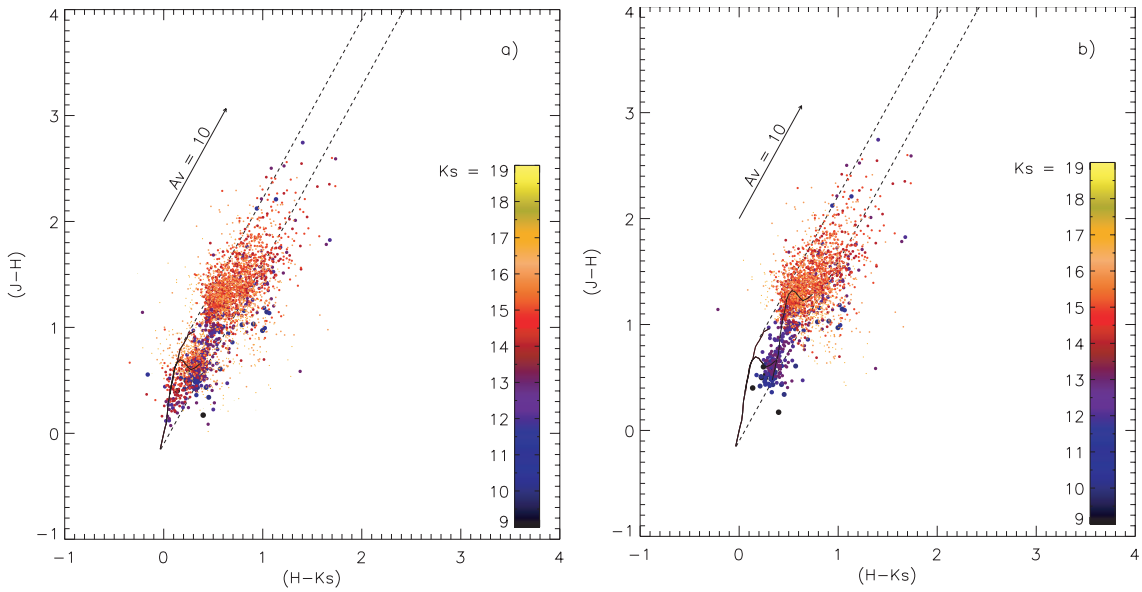

Fig. 9. a) $(H - K_s) - (J - H)$ color−color diagram for the cluster. The color-code and size of the symbol indicates the stars' magnitude. The main-sequence and giant branch are the empiric colors of Bessell & Brett (1988) and the reddening vector is from Rieke & Lebofsky (1985). **b)** Same as panel **a)** without the foreground stars (see text for details). The dark line on the data represents the main sequence shifted by $A_v = 5.8$ mag.

the cluster and are detected in all three bands, which corresponds to a fraction of 11% of the cluster stars. This value is only a lower limit for the excess fraction because (1) J, H, and K_s are not the most sensitive bands to excess emission and (2) our completeness limits correspond to a mass close to 1 $M_\odot$ (see Sect. 4.2) which means we are not sensitive to the excesses of the less massive stars. We would need deep observations in the L band to have a more reliable estimate of this number. For reference, Whitney et al. (2004) report a 26% of stars with excesses using Spitzer survey data, although they note there may be contamination from reddened main-sequence stars and incompleteness in the low-mass end resulting from the bright completeness limits.

In panel *b* of Fig. 9 it is possible to see a small group of 12 bright stars located to the right of the reddening band. Given the generally small photometric errors associated with these bright stars this could be interpreted as the signature of circumstellar matter in the form of envelopes or disks. Four of these stars are isolated and present clear PSFs, two other have good profiles but have relatively close neighbors and the remaining six have either very slightly elongated profiles or are located close to other bright stars. Although this may not be meaningful given that these stars "passed" the error cuts, there is still the possibility that there are other objects within a projected distance smaller than the resolution element of SOFI. If this is not an artifact, these stars should be early B- and possibly even late O-type stars (mass in the range ∼5 to 20 $M_\odot$ for the adopted distance and age, see Fig. 13 in Sect. 4.2). If this excess emission is confirmed by longer wavelength observations (e.g., L-band) this would be suggestive of massive stars having a common formation process to lower mass stars. These stars are mostly seen in projection toward the densest parts of the cluster, which favors their membership, but do not comprise any special structure. These stars may then represent a population of very young, massive stars in this cluster. The fact that they have associated infrared excess emission would not be odd since the bright star to the north of the centre of the cluster (star MSP18 in Fig. 2), identified as an O7 supergiant by Moffat et al. (1991) and as spectral type O4V((f)) by Uzpen et al. (2005), although saturated in our images, presents a large mid-IR excess (Uzpen et al. 2005). In our frames this star appears to be the main member of a small cluster of stars, presumably a more recent site of star formation that we speculate could have been triggered by the main star formation event, the formation of W2. Moreover, Fig. 1 clearly shows large amounts of dust in the form of dark patches to the West of the cluster, indicating that there is still enough material in the cloud, and particularly near the cluster, to have ongoing star formation.

The bright stars located at high reddening are probably distant background giants seen through the cluster's nebula and left-over molecular cloud.

3.4. K-luminosity distribution

Given the delicate position of the cluster in the tangent of the Sagittarius-Carina spiral arm the contamination of the science field is significant and must be accounted for. We did this by statistically subtracting the foreground and background objects estimated by a nearby field observed with the same exposure as the science frames so that it has the same depth. The control field observed for this analysis lies at the same galactic latitude as the cluster, at an angular distance of 1°.65. Ideally the control field should be clear from extinction, but such field was not possible to obtain for this rather complex region of the Galaxy. Figure 10 shows the $(J - H) - (H - K_s)$ color−color diagram for the control field (*grey dots*) where we can clearly see the large range of extinction toward individual stars. The overplotted colors of a circular $20' \times 20'$ 2MASS field (*black dots*) centered on the cluster but excluding the sources located inside the science field area show the contamination to be spread across a large area indicating that the situation would most likely not be improved by the choice of another field. Again, only the sources from 2MASS with quality flags A or B were selected. Figure 10 illustrates well how difficult it is to find an unreddened control field along a spiral arm tangent. There are too many molecular clouds to be able to find an extinction-free line-of-sight. Still, this control field is the best representation of the reddened/unreddened foreground/background stellar population toward W2 and we will use it as such in the following analysis.

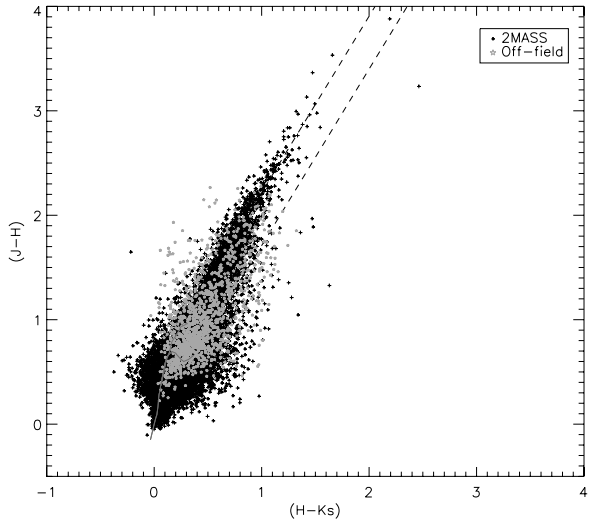

Fig. 10. $(H - K_s) - (J - H)$ color−color diagram for the control-field (*grey dots*) and for a larger 2MASS field (*black dots*). Both the fields present a significant amount of extinction.

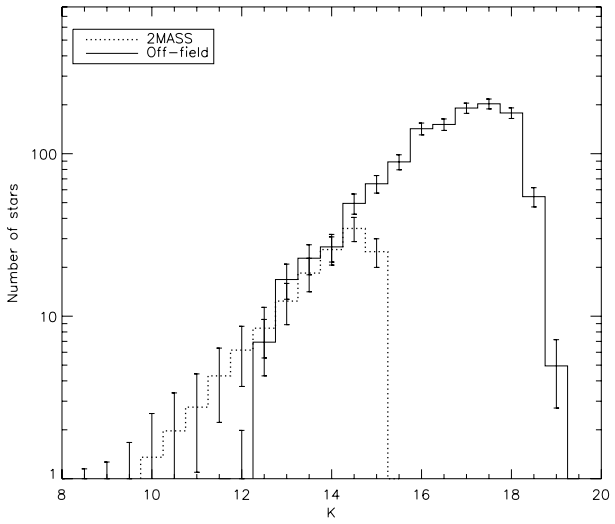

Fig. 11. K_s differential luminosity function for the 2MASS field *(dotted line) and the control field (solid line). The KLFs were appropriately scaled to the area of the science field.*

Since we only observed a control field for the long exposures we lack information about the contamination in the range of magnitudes K_s = 9.2 mag to 11.3 mag. This was overcome by combining the information in the 2MASS control field for the bright objects and our control field for the faint. In Fig. 11 we present the comparison between the K_s-luminosity function (KLF) for our control field and the 2MASS field. The KLFs were both appropriately scaled to the area of the science frame to account for the different sizes of the fields of view. The completeness limits available in the literature for 2MASS are highly dependent on the galactic latitude and are not specified for this particular region. Since we know our sample to be complete up to K_s = 15.5 mag it is reasonable to assume the 2MASS field to be complete as far as the histograms overlap, which happens until the K_s = 14 mag bin considering the error bars. We therefore use the information from 2MASS up to this bin, because it covers a larger area hence having a higher signal-to-noise, and the information from our control field for fainter objects.

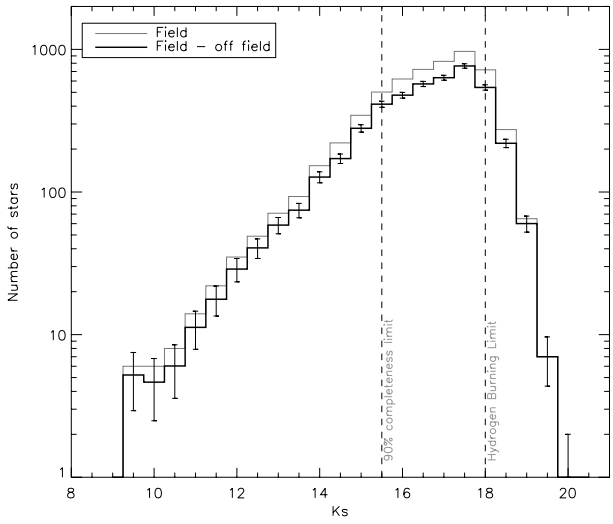

Fig. 12. KLF for the cluster before (*light line*) and after (*dark line*) the control-field subtraction. The vertical dashed lines indicates the 90% completeness limit for the sample and the hydrogen burning limit for the derived distance and age (see Sect. 4.1).

The cluster's differential KLF is presented in Fig. 12 before (*light line*) and after (*dark line*) the control field subtraction. The brightest non-saturated star in our sample has K_s = 9.25 mag. According to this KLF, 4516 of the stars in the field should belong to the cluster. Although this is merely a lower limit for the total number of cluster members given the relatively high completeness limit, this is the most extensive catalog so far for this cluster.

4. Analysis and discussion

4.1. Age and distance

The distribution of fainter stars in the CMD (Fig. 8) shows a great deal of structure that can be used to constrain the distance and age of the cluster to some extent. The most prominent feature in the CMD is the presence of a vertical concentration around $(J-K_s) \sim 1.8$ mag (*panel a* of Fig. 8) that traces the set of Hayashi tracks, the first and convective stages of contraction of the pre-main-sequence (PMS) for stars less massive than 2.5 $M_\odot$ (Stahler & Palla 2005). These vertical, descending tracks do not separate well in $(J - K_s)$ for the different masses, causing the PMS stars in these stages to concentrate on a narrow range of color and rendering the bulk of this region almost useless for the determination of distance and age. What we can use, however, is its brighter limit to infer an upper estimate for the distance as we know the age of these objects cannot be smaller than zero. If the brightest PMS stars are on the birthline (have an age of zero) the empirical PMS models of Palla & Stahler (1993) imply a distance smaller than 3.7 kpc. Nevertheless, we note that this is an unlikely upper limit because (1) the centre of the cluster is almost clear of material as can be assessed by the fact that it is already visible at optical wavelengths, (2) the excess fraction in the cluster is very low and (3) the cluster is highly compact and nearly spherical, suggesting some degree of dynamical relaxation. Regarding the first point, assuming a typical star formation efficiency of a few percent, the amount of gas and dust necessary to form a cluster as massive W2 (see Sect. 4.2) should be of the order of several times 10^5 $M_\odot$ to 10^6 $M_\odot$. For very young ages one would therefore expect, comparatively, a more

embedded cluster, with a larger amount of differential reddening, as in the case of Trapezium cluster (Muench et al. 2002).

After completing the homologous contraction along the Hayashi tracks a PMS object continues its path toward the zero age main sequence (ZAMS) along the Henyey tracks. These mark the growth of radiative cores in the contracting objects and are roughly horizontal in the CMD, comprising a bridge between the Hayashi track area and the main sequence (MS). In the case of a coeval population, the data in this transition region would therefore be distributed along a specific isochrone in the form of a single horizontal arc leaving the remaining transition region unpopulated. The data from W2 presents at least two such arcs, as well as some diffuse "inter-arc" objects suggesting continuous star formation perhaps marked by (at least) two relatively well defined episodes. The brightest of these arcs ($K_s \sim 13$ mag) becomes very prominent when we highlight the sources only from the central regions (*panels b* and *c* of Fig. 8), in this case from a 1′-side square centred in the peak of the stellar density distribution. At the minimum distance available in the literature for W2 (2.3 kpc, Brand & Blitz 1993) this arc would correspond to the 2.6 ± 0.1 Myr isochrone, setting this value as the age of the youngest stellar population in the cluster. Although marginally compatible with the presence of the O7V stars found by Moffat et al. (1991) in the cluster core, this age does not accommodate the presence of the O6V stars found by the same authors and even less that of the O4V star suggested by Uzpen et al. (2005)[3]. We therefore adopt an intermediate distance of 2.8 kpc, the value that best suits a minimum age between 1.5 and 2 Myr (the lifetime of an O4 to O6 star in the MS) for the arc. We are assuming this arc to represent the most recent *global* event of star formation, which does not exclude the eventual formation of individual stars after this period.

The poor knowledge of distance is a source of uncertainty when comparing model isochrones to the data. The effect of distance is a shift of the isochrones in magnitude (i.e., vertically) as determined by the distance modulus equation:

$$m - M = -5 + 5 \log d \tag{10}$$

$$m_{d_1} = m_{d_2} + 5 \log (d_1/d_2) \tag{11}$$

where M is the absolute magnitude and m, m_{d_1} and m_{d_2} are the apparent magnitudes at distances d (pc), d_1 and d_2 respectively. For this reason all the ages determined in this paper will be affected if the true distance to the cluster is different from 2.8 kpc. For this distance we estimate the age of the cluster core (as traced by the aforementioned arc) to be 2.0 ± 0.3 Myr (*panel c* of Fig. 8). We still find a significant population above (brighter) this arc, made up mostly by stars which are not far from the core. These may represent a yet younger (0.7 ± 0.3 Myr) population or may simply reflect the statistical effects of binarity associated with the 2 to 3 $M_\odot$ stars that populate the $K_s \sim 13$ mag arc. The other prominent arc is one magnitude fainter ($K_s \sim 14$ mag, *panel d* of Fig. 8) and is well fit by isochrones between 3.0 and 4.8 Myr, suggesting either continuous star formation over this period or a star formation episode somewhere in this range.

Regarding the PMS isochrone fitting we note that the exact shape of each isochrone is not provided by the models because they are poorly sampled in mass. Although we could make an educated guess about the shape of a given isochrone considering the different evolutionary times and interpolating carefully over the absent masses, we chose not to do so to avoid a "fit by hand" that would be difficult to explain. Instead, we have used a numerical interpolation of a quadratic function to draw the line that joins the model points (*panels c* and *d* of Fig. 8). The close groups of points over the isochrones contain the color and magnitude for the same mass over the range of ages that fit each arc. Despite our efforts to build "correct" isochrones, we still expect the real isochrone in *panel c* to be broader than the plotted line especially toward redder colors for $K_s < 14$ mag, thus composing a better fit to the data. Also, in *panel d*, the unnatural bump in the isochrone close to $K_s \sim 14.3$ mag is caused by the fact that we include information regarding the range of possible ages rather than the information about a single age.

Alternatively, one could estimate the age of the cluster by knowing the extinction, the distance, and the spectral types of some of its stars using the method of spectral parallax. In this case, the comparison between the model and observed brightness for the corresponding spectral types would yield the age. Moffat et al. (1991) have identified a few O7V and O6V stars in the cluster based on optical spectroscopy. Of these we have photometry for two of the O7V stars (hereafter MSP167 and MSP203) and two of the O6V stars (hereafter MSP151 and MSP157), all identified in Fig. 2. This classification is somewhat in conflict with our photometry in the sense that (1) there is a difference of $K_s \sim 0.7$ mag between the two O7V stars that cannot be explained by our photometric error bars and (2) the two stars identified as O6V are fainter than the ones identified as O7V contrary to what is expected. Star 203 of Moffat et al. is one of the stars that possibly presents NIR excess in the CC diagram (see Sect. 3.3). Nevertheless, if the spectral classification of Moffat et al. (1991) for the O7V stars is accurate, then they would be, according to the models of Lejeune & Schaerer (2001)[4], between 1 and 3 Myr for a distance of 2.8 kpc respectively. As mentioned earlier, Uzpen et al. (2005) classify star MSP18 (Fig. 2) as an O4V star, which represents a discrepancy of three subclasses with respect to the classification of Moffat et al. Although this is a particular star with clear IR excess that can lead to misidentifications, if the same tendency was to be applied to the other stars, the ages derived in this way would be significantly underestimated for whatever adopted distance.

Binarity may be an important caveat to our results: if most stars in the sample are in binary or multiple systems, our distance may be underestimated as we are assuming them to be brighter than they actually are. The effect of unresolved binaries could explain the vertical scatter relative to each of the arcs. In the worst case scenario binaries will be 0.75 mag brighter than a single star, which corresponds to a maximum increase of 1 kpc in distance for the unlikely case of all or the vast majority of stars in the arcs are in equal-mass binary systems.

All these points considered, we adopt a distance to the cluster of 2.8 kpc and an age of $\sim 2 \pm 1$ Myr for the cluster core with the possibility of coexistence with a younger (less that 1 Myr) and/or an older (up to 4.8 Myr), possibly more extended populations.

The distances we estimate for W2 are well within the limits found in the literature, although they are in better agreement with the lowest values, especially the one derived by Brand & Blitz (1993) – 2.3 kpc – based on velocity fields for the Galaxy (see discussion of distances in Sect. 1). We consider our estimate to

[3] According to Massey (2003) a 40 $M_\odot$ O6 star will spend less than 2 Myr in the MS, whereas a 60 $M_\odot$ O4 star will reach the giant phase in less than 1.5 Myr.

[4] The magnitudes and colors from the models were converted into spectral types by assuming the luminosity scale from Vacca et al. (1996) and matching it with the predicted model luminosities. For approximately the same luminosities, the effective temperatures from the models Lejeune & Schaerer (2001) are generally underestimated with respect to Vacca et al.

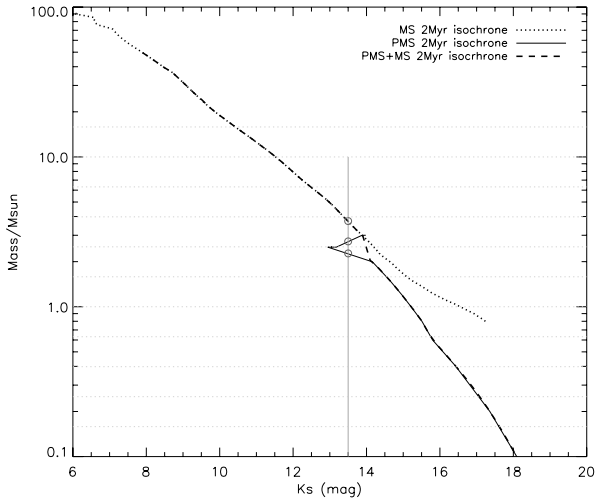

Fig. 13. Mass-luminosity relation for an age of 2 Myr and a distance of 2.8 kpc. The *dotted* and *solid lines* represent the MS and PMS MLR respectively. The *dashed line* represents the final MLR used to derive the mass function. The *light vertical line* at $K_s = 13.5$ mag illustrates the triple degeneracy in the MLR. The *horizontal dotted lines* limit the mass bins used for the mass function.

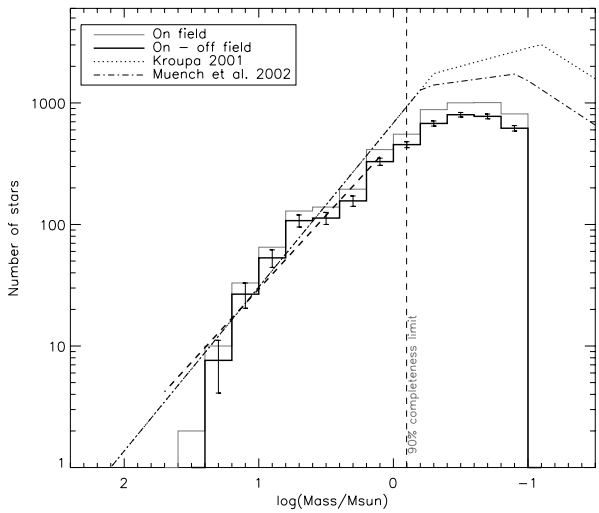

Fig. 14. Mass function for the cluster before (*light line*) and after (*dark line*) the control-field subtraction. The linear fit to the histogram for $M > 1\ M_\odot$ is represented by the dashed line.

be quite robust as it is based on good statistics rather than a small number of stars and uses the more appropriate PMS tracks to fit the data instead of the main-sequence or ZAMS. The excellent agreement of the models with the data is a good indicator that the underlying physics in these models is capturing the essence of the star formation process.

4.2. Mass distribution

We derived an approximate mass function (MF) for the cluster from the KLF (Sect. 3.4) by assuming a given mass-luminosity relation (MLR). Our ML relation (Fig. 13) was constructed from the 2-Myr isochrones from Palla & Stahler (1993) for masses between 0.1 and 2 $M_\odot$ and from Lejeune & Schaerer (2001) for higher masses.

As seen in Sect. 3.2 we have both main sequence and pre-main sequence objects in the sample. If we forget, for now, the foreground main sequence sources (blue plume in panels *a* and *d* of Fig. 8) we can divide the extracted sources into a well defined PMS sources region ($K_s > 14.2$ mag) and MS sources region ($K_s < 12.7$ mag). For this reason it is fair to construct a MLR based on the PMS tracks for the first and the MS tracks for the latter. However, for the sources with intermediate brightness, the case is not clear cut as MS objects with 3 to 5 $M_\odot$ will have the same brightness as PMS objects with 2 to 3 $M_\odot$ (see Fig. 13). Furthermore, still in this range of brightness, the $2.5 < M/M_\odot < 3$ PMS objects have already begun the hydrogen burning through the CNO bi-cycle and have developed a convective core making them, at this time, fainter than the $2 < M/M_\odot < 2.5$ PMS objects still in the *Henyey* track (see chap. 16 of Stahler & Palla 2005, for a discussion of the physical phenomena involved). This adds yet another level of ambiguity to the MLR in this range of masses (Fig. 13). Since we have no way to separate the sources appropriately in order to lift the triple degeneracy and create a one-to-one correspondence between the mass and the K_s-luminosity of the sources, we chose to consider all sources brighter than $K_s = 14$ mag as MS objects thus obtaining the MLR represented by the *dashed line* in Fig. 13. In this way we are overestimating the mass of the 2 to 3 $M_\odot$ PMS objects by as much as 2.5 $M_\odot$ thus underestimating the number of stars with mass between 2 and 3 $M_\odot$ while overestimating the number of stars in the range of 3 to 5 $M_\odot$. We note that in order to be more robust, the following mass-function analysis should be reassessed in a more accurate manner similarly to what was done for the Trapezium by Muench et al. (2002).

We applied this MLR to our list of K_s magnitudes for the surveyed science and control fields and constructed the mass function for the sample. Figure 14 shows the mass function before (*light line*) and after (*dark line*) the control field subtraction. Given the young age of the cluster, this should roughly correspond to the cluster's initial mass function (IMF). Assuming the same distance (2.8 kpc) for the whole sample, we are overestimating the mass of the foreground stars as they appear brighter. However, since we adopt the same distance for the cluster and control fields, those foreground sources should statistically cancel out in the control field subtraction. Should the distance be greater than our derived value, all the masses in the following analysis would be underestimated by a factor of $(\frac{d(\mathrm{kpc})}{2.8})^2$.

The best linear fit to the mass function above the completeness limit (~0.8 $M_\odot$) yields a slope of -1.20 ± 0.16 (*dotted line* in Fig. 14). Given all the approximations made in building this mass function this value is surprisingly compatible with the Salpeter (1955) slope of −1.35. Since we are only detecting a small fraction of the faint stars in the crowded centre, the low-mass bins are likely underestimated, which means that the real slope should be slightly steeper. The high completeness limit of our sample does not allow for any conclusion about the turn-off point or the behavior of the mass function beyond 0.8 $M_\odot$.

The slight deficit of sources in the $\log(M/M_\odot) = 0.3$ and 0.5 bins and the small "bump" in the $\log(M/M_\odot) = 0.7$ bin are a consequence of the MLR as discussed above. We have performed several tests and concluded that the inaccuracy and the artifacts introduced by the mixed population of MS and PMS objects and the subsequent choice of MLR are not large enough to influence the slope of the MF or the scaling of the Kroupa (2001) and Muench et al. (2002) IMFs within the error bars.

The integration of the cluster's MF without corrections for completeness or saturated stars yields a total mass of 3756 $M_\odot$, 2809 $M_\odot$ of which lie within the completeness limit. This limit is set for the faint end but does not account for the brighter

saturated stars in our sample. For this reason, we can say our mass estimate is complete only from the mass that corresponds to the level of saturation which, in turn, depends on the exposure time, thus having different values for the long and short exposures fields. Therefore, for the sake of completeness in the higher masses, we can count the saturated stars and estimate a lower limit of their contribution to the mass. We count three saturated stars in the short exposure frames. For these exposures the saturation level is $K_s = 9.25$ mag which, at the assumed distance, corresponds to a mass of 25 $M_\odot$, so the three stars should add a mass of at least 75 $M_\odot$ to the previously derived values. In the long exposures we count twenty-nine saturated stars, of which we will exclude the Wolf-Rayet binary WR20a whose combined mass was measured to be ∼160 $M_\odot$ (Rauw et al. 2005). The long exposures have a saturation level around $K_s = 11.33$ mag, which corresponds to a mass of 11 $M_\odot$. The remaining twenty-eight stars will then add at least 308 $M_\odot$ to the total mass. Putting everything together (including the WR binary) we obtain an extra 543 $M_\odot$ yielding a total mass larger than 4299 $M_\odot$ for the detected sources. The stars with $M > 1$ $M_\odot$ should therefore comprise at least 3352 $M_\odot$ of the total mass of the cluster. Since we do not have the precise estimate for the mass of the saturated stars we did not include them in the MF but we note that their presence should add at least one mass bin to the histogram (relative to the short exposures saturation limit) and possibly increase the higher-mass existing bins.

If we assume a field IMF as defined by Kroupa (2001) given by the equation

$$\alpha = \begin{cases} -1.3 & M/M_\odot \geq 0.5 \\ -0.3 & 0.08 \leq M/M_\odot < 0.5 \\ 0.7 & 0.01 \leq M/M_\odot < 0.08 \end{cases} \quad (12)$$

where

$$\frac{\mathrm{d}\log N}{\mathrm{d}\log M} \propto M^{-\alpha} \quad (13)$$

to be a good representation of the mass distribution in the cluster and scale it appropriately, we will obtain a correction for the higher ($M > 1$ $M_\odot$) masses of 719 $M_\odot$, relatively close to our lower estimate, and a total mass of 7004 $M_\odot$. Within the uncertainties, that easily change this estimate by a factor of two, the derived stellar cluster mass is of the same order of magnitude of the most massive clusters known in the Galaxy, namely W49A ($5-7 \times 10^4$ $M_\odot$, Homeier & Alves 2005), the Quintuplet cluster (6.3×10^3 $M_\odot$, Figer et al. 1999), Arches (2×10^4 $M_\odot$, Figer 2005), NGC 3603 (7×10^3 $M_\odot$, Stolte et al. 2004, 2006), or Westerlund 1 (5.6×10^4 $M_\odot$, Clark et al. 2005). However, contrary to the results of Figer et al. (1999) for the Quintuplet and Stolte et al. (2006) for NGC 3603, we do not find evidence for a top-heavy mass function.

For a cluster this massive, the above IMF predicts the most massive star to be 126 $M_\odot$. One would therefore expect to find 13 stars brighter than our highest saturation limit ($K_s = 9.25$ mag, $M \sim 25$ $M_\odot$). From the 29 stars saturated in the long exposures and not present in the short exposures we believe that 7 at least are brighter than this limit. If we add the three stars saturated in the short exposures we would still have a deficit of 3 (±1.7) stars more massive than 25 $M_\odot$. The fact that we do not observe them indicates that they were either not formed or already evolved into supernovae. Interestingly, X-ray studies performed by Goldwurm et al. (1987) consider the possibility of an X-ray bubble associated with the cluster being powered by a supernova remnant, an event which could indeed be powerful

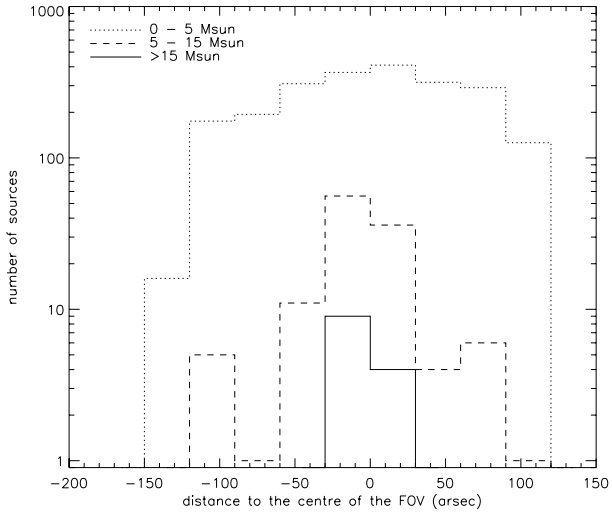

Fig. 15. Spatial distribution of stars of different masses in the SOFI field. The *x*-axis represents the distance in declination to the centre of the field of view.

enough to produce such an effect. More recently, the analysis of Townsley et al. (2005) reveal the presence of a non-thermal component in their *Chandra* X-ray data that they interpret as the possible signature of a supernova remnant. Even though it is known that a cluster of high mass stars alone can power such a bubble one cannot rule out the possibility of a supernova being the source of energy. In our images we cannot see the presence of a remnant but the "missing stars" in the mass function hint at its presence. In order to settle this issue it is necessary to establish the membership of WR20a as well as to conduct a deeper energy analysis of the area.

In this sense we would still like to comment on the position of WR20a (see Fig. 2). This binary lies 35.″5 (0.5 pc at a distance of 2.8 kpc) away from the centre of the cluster and appears in the literature as a likely cluster member given its proximity to the centre of the cluster and the rarity of such objects (Moffat et al. 1991; Carraro & Munari 2004; Whitney et al. 2004; Rauw et al. 2005). As it would be difficult to explain the process by which it might have been ejected from the centre of the cluster where it might have formed it is also hard to miss the coincidence that the most massive central stars are organized in a bean-shaped structure that opens exactly in the direction of WR20a. If indeed an extremely energetic phenomenon has occurred in the past somewhere between what is now the cluster and WR20a we might expect the kick to be strong enough to open a cavity in the central concentration ejecting at the same time the massive binary. This would be supported by the fact that the binary is not clustered as one would expect if it was the centre of another site of massive star formation. Although this analysis is merely speculative, we can entertain this idea further by recalling the X-ray studies described in the previous paragraph.

Finally, regarding mass segregation, Fig. 15 shows the distribution in declination of the different mass stars in our field of view. The distribution of the lower mass (<5 $M_\odot$) stars decays very gradually toward the outer edges of the image, although the plot suggests that it continues to spread for an area wider than our image. The steeper decline of the distribution to the south reflects the presence of the bright ionized shell of gas that sets the detection limit to brighter values. The intermediate mass (5–15 $M_\odot$) stars concentrate mostly in the inner 3.′5 and the most massive stars are located in the inner 1′, except for the

WR binary (not plotted here because it is saturated in our sample) that lies well outside this range. These distributions strongly favor mass segregation in the sense that the massive stars appear to concentrate toward the cluster core. These data are inconclusive regarding the distribution of low mass stars in this region given the high source detection threshold in the crowded centre. However, it is clear that we do not observe a deficit of these stars in the core with respect to the outer regions.

5. Conclusions

We have analysed near-IR JHK_s photometric data of the inner $\sim 3'.9$ of the Westerlund 2 embedded cluster and derived a set of basic parameters for the cluster. Our sample is complete up to 1 $M_\odot$, although our sensitivity limit goes well below the hydrogen burning limit. The parameters we derive are the following:

- By comparison with main- and pre-main-sequence tracks we derive a mean global extinction of $A_v = 5.8 \pm 0.8$ mag toward the cluster and an intra-cluster extinction that does not generally exceed 10 mag.
- We find a distance to the cluster of 2.8 kpc and an age of 2.0 ± 0.3 Myr for the core of the cluster, although we cannot exclude the possibility of continuous star formation over a period of the order of 3 Myr for a area larger than the core of the cluster.
- The fraction of sources that present JHK_s excess emission is 11% of the cluster sample, a lower limit to the actual fraction given the high completeness limits and the fact that these bands are not ideal for excess studies.
- The mass function for this cluster is compatible with a Salpeter power-law until completeness (slope of -1.20 ± 0.16) and the total mass, as estimated by the extrapolation of a scaled field IMF, amounts to 7004 $M_\odot$. This IMF predicts the existence of a 125 $M_\odot$ star that we do not observe in our images. We find no evidence for a top-heavy mass function.
- We find compelling evidence for spatial segregation of the massive stars that are found to concentrate toward the core of the cluster.

We have also analysed the 2MASS data for this cluster to try to determine its physical extent. By comparison with our data, we find the 2MASS catalog for this region to be complete up to $K_s = 14$ mag. Although the data are not ideal, we find the radius of the cluster, as given by 2MASS $K_s < 14$ mag stars, not to extend beyond $5'$.

Acknowledgements. We would like to thank Valentin Ivanov for the help during observations and the anonymous referee for the corrections and suggestions. We are particularly grateful to August Muench for the valuable discussion and relevant comments. J. Ascenso acknowledges financial support from the Portuguese institution FCT (Fundação para a Ciência e Tecnologia) through grant number SFRH/BD/13355/2003 and the warm hospitality of ESO Garching as host institution during part of this work.

References

Alves, J., & Homeier, N. 2003, ApJ, 589, L45
Bessell, M. S., & Brett, J. M. 1988, PASP, 100, 1134
Brand, J., & Blitz, L. 1993, A&A, 275, 67
Carpenter, J. M. 2001, AJ, 121, 2851
Carraro, G., & Munari, U. 2004, MNRAS, 347, 625
Caswell, J. L., & Haynes, R. F. 1987, A&A, 171, 261
Churchwell, E., Whitney, B. A., Babler, B. L., et al. 2004, ApJS, 154, 322
Clark, J. S., Negueruela, I., Crowther, P. A., & Goodwin, S. P. 2005, A&A, 434, 949
Eisenhauer, F., Quirrenbach, A., Zinnecker, H., & Genzel, R. 1998, ApJ, 498, 278
Figer, D. F. 2005, Nature, 434, 192
Figer, D. F., Kim, S. S., Morris, M., et al. 1999, ApJ, 525, 750
Gianotti, H. F., Quiroga, R. J., & Varsavsky, C. M. 1972, Ap&SS, 17, 126
Goldwurm, A., Caraveo, P. A., & Bignami, G. F. 1987, ApJ, 322, 349
Goss, W. M., Radhakrishnan, V., Brooks, J. W., & Murray, J. D. 1972, ApJS, 24, 123
Gum, C. S. 1955, MmRAS, 67, 155
Homeier, N. L., & Alves, J. 2005, A&A, 430, 481
Kroupa, P. 2001, MNRAS, 322, 231
Kumar, M. S. N., Ojha, D. K., & Davis, C. J. 2003, ApJ, 598, 1107
Lada, C. J., & Lada, E. A. 2003, ARA&A, 41, 57
Lada, C. J., Alves, J., & Lada, E. A. 1996, AJ, 111, 1964
Lejeune, T., & Schaerer, D. 2001, A&A, 366, 538
Liu, W. M., Meyer, M. R., Cotera, A. S., & Young, E. T. 2003, AJ, 126, 1665
Manchester, R. N., Robinson, B. J., & Goss, W. M. 1970, Aust. J. Phys., 23, 751
Massey, P. 2003, ARA&A, 41, 15
Moffat, A. F. J., & Vogt, N. 1975, A&AS, 20, 125
Moffat, A. F. J., Shara, M. M., & Potter, M. 1991, AJ, 102, 642
Muench, A. A., Lada, E. A., Lada, C. J., & Alves, J. 2002, ApJ, 573, 366
Palla, F., & Stahler, S. W. 1993, ApJ, 418, 414
Persson, S. E., Murphy, D. C., Krzeminski, W., Roth, M., & Rieke, M. J. 1998, AJ, 116, 2475
Piatti, A. E., Bica, E., & Claria, J. J. 1998, A&AS, 127, 423
Piskunov, A. E., Belikov, A. N., Kharchenko, N. V., Sagar, R., & Subramaniam, A. 2004, MNRAS, 349, 1449
Rauw, G., Crowther, P. A., De Becker, M., et al. 2005, A&A, 432, 985
Rieke, G. H., & Lebofsky, M. J. 1985, ApJ, 288, 618
Rodgers, A. W., Campbell, C. T., & Whiteoak, J. B. 1960, MNRAS, 121, 103
Salpeter, E. E. 1955, ApJ, 121, 161
Shara, M. M., Smith, L. F., Potter, M., & Moffat, A. F. J. 1991, AJ, 102, 716
Stahler, S. W., & Palla, F. 2005, The Formation of Stars, by Steven W. Stahler, Francesco Palla (Wiley-VCH), 865
Stolte, A., Brandner, W., Brandl, B., Zinnecker, H., & Grebel, E. K. 2004, AJ, 128, 765
Stolte, A., Brandner, W., Brandl, B., & Zinnecker, H. 2006, AJ, 132, 253
Townsley, L., Feigelson, E., Montmerle, T., et al. 2005, in X-Ray and Radio Connections, ed. L. O. Sjouwerman, & K. K Dyer, Published electronically by NRAO, http://www.aoc.nrao.edu/events/xraydio Held 3–6 February 2004 in Santa Fe, New Mexico, USA (E3.04), 10 pages
Uzpen, B., Kobulnicky, H. A., Olsen, K. A. G., et al. 2005, ApJ, 629, 512
Vacca, W. D., Garmany, C. D., & Shull, J. M. 1996, ApJ, 460, 914
Westerlund, B. 1961, Arkiv Astron., 2, 419
Whiteoak, J. B. Z., & Uchida, K. I. 1997, A&A, 317, 563
Whitney, B. A., Indebetouw, R., Babler, B. L., et al. 2004, ApJS, 154, 315
Wilson, T. L., Mezger, P. G., Gardner, F. F., & Milne, D. K. 1970, A&A, 6, 364